Optical and Quantum Electronics (2026) 58:124
https://doi.org/10.1007/s11082-026-08711-9

Enhanced performance salinity sensor based on dual-wavelength laser speckle correlation

Carlos Angulo Barrios[1]

Received: 9 June 2025 / Accepted: 3 February 2026

Abstract
This paper presents a simple signal processing procedure to enhance the performance of a free-space laser speckle-based salinity sensor system. The experimental setup comprises a cylindrical glass vessel containing the liquid sample of interest, which is probed by a light beam formed by merging two laser beams of different wavelengths. The mixed laser beam produces a speckle pattern that provides quantitative information on the sample concentration by correlation coefficient determination. The definition of a multiplicative fusion function, which involves the multiplication of the measured correlation coefficients for each two wavelengths, enhances the sensor's sensitivity compared to a single-wavelength approach without altering the system noise, thereby increasing the signal-to-noise ratio. The combined product function allows the sensor system to exhibit high linearity at low concentrations, an enlarged output range, a salinity sensitivity of -0.853 /%, which is significantly higher than that reported for fiber optic speckle-based salinity sensors, and a limit of detection comparable to that offered by state-of-the-art, more complex, interferometer-based optical fiber salinity sensors.

Keywords Optical sensor · Salinity measurement · Laser speckle · Correlation coefficient · Dual-wavelength

1 Introduction

Salinity is a critical indicator of water quality (https://www.watereducation.org/water-academy). The measurement of the salt content in water is of great importance in key socio-economic sectors such as health, industrial production, food industry, agriculture, and marine environmental monitoring. Among the various salts, the measurement of NaCl concentration in water is particularly important for many fields. In a medical context, NaCl plays a pivotal role in treating fluid loss and maintaining electrolyte balance − a critical aspect

✉ Carlos Angulo Barrios
carlos.angulo.barrios@upm.es

[1] Department of Photonics and Bioengineering, CEMDATIC, ETSI Telecomunicación, Universidad Politécnica de Madrid, Ciudad Universitaria s/n, Madrid 28040, Spain

Published online: 11 February 2026

of patient care −, particularly for those unable to consume nutrients and fluids orally (de Felippe et al. 1980). From a nutritional standpoint, NaCl is indispensable in regulating body water levels (Rakova et al. 2017) and maintaining optimal blood pressure (Nho et al. 1998), a salient issue for individuals of middle and advanced age with a family history of hypertension. In addition, NaCl is a key ingredient in many food products, where it is used to enhance flavor and extend the shelf-life of food items (Brul and Coote 1999). Notably, NaCl is the main component of inorganic salts found in seawater, with a concentration several orders of magnitude higher than that of other salts (Huber et al. 2000).

Current salinity sensors are primarily based on two methods: electrical and optical. Salinity electrical sensors typically rely on the measurement of water conductivity (Ramos et al. 2008; Carminati and Luzzatto-Fegiz 2017; Cloete et al. 2016). This is a practical and widely used method; however, it necessitates the immersion of a probe into the sample, which can result in probe corrosion and sample contamination. Salinity optical sensors are mainly based on measuring the refractive index, as there is a well-established relationship between refractive index and salt concentration of aqueous solutions (Li et al. 2015). Optical sensors do not require direct contact with the sample, are immune to electrical interferences, and provide very high sensitivities. This has led to significant research efforts in developing salinity-sensing systems based on optical technologies. These include free-space configurations, such as those based on laser beam displacement in a refractometric cell (Zhao et al. 2003a, b; Malarde et al. 2008), and fiber optics-based configurations (Luo et al. 2017; Pereira et al. 2004; Wu et al. 2020; Possetti et al. 2009; Yu et al. 2019; Wang and Chen 2012; Gentleman and Booksh 2006; Nguyen et al. 2010; Meng et al. 2014; Wu et al. 2011, Guzman-Sepulveda et al. 2013; Lin et al. 2021).

Speckle-based optical sensors are of particular relevance due to their ability to provide simple, cost-effective, and sensitive solutions for a variety of applications. Speckle is defined as a granular optical intensity pattern that emerges when highly coherent light is scattered by a random structure or when multiple modes within an optical fiber interfere as they propagate and emerge from the fiber. Speckle patterns exhibit a high sensitivity to light phase differences, rendering them well-suited for use in both free-space and fiber optic sensing configurations for measuring a wide range of parameters, including refractive index (Trivedi et al. 2019; Tran et al. 2020; Facchin et al. 2022; Arı et al. 2023; Barrios 2024), vibration (Pinzon et al. 2017), roughness (Sprague 1972), strain (Pan and Yu 1995; Fujiwara et al. 2018), velocity (Barker and Fourney 1977), displacement (Chen et al. 2019), and biomolecular hybridization (Feng et al. 2018). These sensors utilize speckle patterns to establish a relationship, typically the correlation coefficient, between the speckle image of a reference sample and that corresponding to the sample under test. The employment of a simple CCD camera for speckle imaging, instead of sophisticated and costly optical spectrum analyzers, enables the acquisition of the sensing signal, thereby reducing expenses and complexity of the readout instrumentation.

A variety of methods have been proposed to increase the sensitivity of free-space and fiber-optic speckle pattern-based sensing systems. In free-space configurations, the sensitivity of refractive index sensing systems has been enhanced by increasing the number of scattering effects (Tran et al. 2020; Facchin et al. 2022) and by employing optical lensing (Barrios 2024). In the context of fiber-optic configurations, Arı et al. (2023) have shown that the sensitivity of a tapered optical fiber speckle-based refractive index sensor can be improved by optimizing the fiber dimensions. These authors also demonstrated that the

sensor´s sensitivity can be further enhanced by segmenting the speckle images and calculating the mean correlation from all the calculated correlations for each segment. Pinzon et al. (2017) used a dual-wavelength interrogation approach to enhance the vibration sensitivity of a plastic optical fiber (POF). These authors injected two wavelengths into a POF to detect micro-vibrations at specific points of the fiber by analyzing the speckle of the reflected light. Their experiments showed that using the correlation coefficient of the product of the correlation coefficients of the two wavelengths as the sensor response resulted in an increase in fiber vibration sensitivity compared to using the correlation coefficient at a single wavelength, without increasing the measurement uncertainty due to noise.

This work presents a signal processing procedure that enhances the performance of a salinity sensor system based on dual-wavelength laser speckle correlation. In contrast to the work referenced in (Pinzon et al. 2017), this approach utilizes a dual-wavelength interrogation in a free-space configuration. In this configuration, a red laser beam and a green laser beam are mixed into a single beam to probe the sample under test, and the speckle is formed by illumination of a diffusive random surface. The mixed two-wavelength speckle pattern is captured using a digital camera, and an acquisition program computes the correlation coefficients corresponding to the red and green color components of the speckle image simultaneously. The correlation coefficients of these color components are multiplied to generate a combined product correlation signal, which constitutes the response of the sensing system. The performance of the sensor based on this fusion function approach is discussed in comparison with the use of a single-wavelength technique in terms of sensitivity, noise, limit of detection, linearity, and dynamic range.

2 Materials and methods

The studied configuration is based on the refractometric sensor using laser speckle correlation and lensing described in (Barrios 2024), which provides detailed information on its operation. In essence, a laser beam passes through a glass cylindrical pipette containing the liquid sample of interest and is incident on a diffuser, which generates a speckle pattern in transmission that is captured by a CCD camera. The alterations in the sample refractive index are determined by measuring the correlation coefficient between the speckle patterns of a reference sample and the test sample. The primary innovation in the optical setup of the present work is the incorporation of a second interrogation laser beam for enhancing the system performance.

Figure 1 shows a schematic diagram (a) and a photograph (b) of the salinity sensing system. A CW 635-nm-wavelength (red) laser diode (World Star Tech TECRL-635) and a CW 532-nm-wavelength (green) diode pumped solid-state laser (CW532-04–5 from Roithner Lasertechnik) were used as light sources. A glass slide was used as a beam combiner to merge both laser beams into a common beam, and the intensity of the combined beam was controlled by a variable optical attenuator (VOA). The attenuated laser beam was then directed onto a vertically positioned glass Pasteur pipette (outer diameter = 6.5 mm, inner diameter = 5.1 mm) at a point approximately 1 mm from its optical axis. A syringe was used to introduce or remove liquid samples into or from the pipette through a flexible pipe (PharMed BPT Saint Gobain Performance Plastics™) connected to the bottom aperture of the pipette. An iris diaphragm positioned between the VOA and the pipette was utilized to

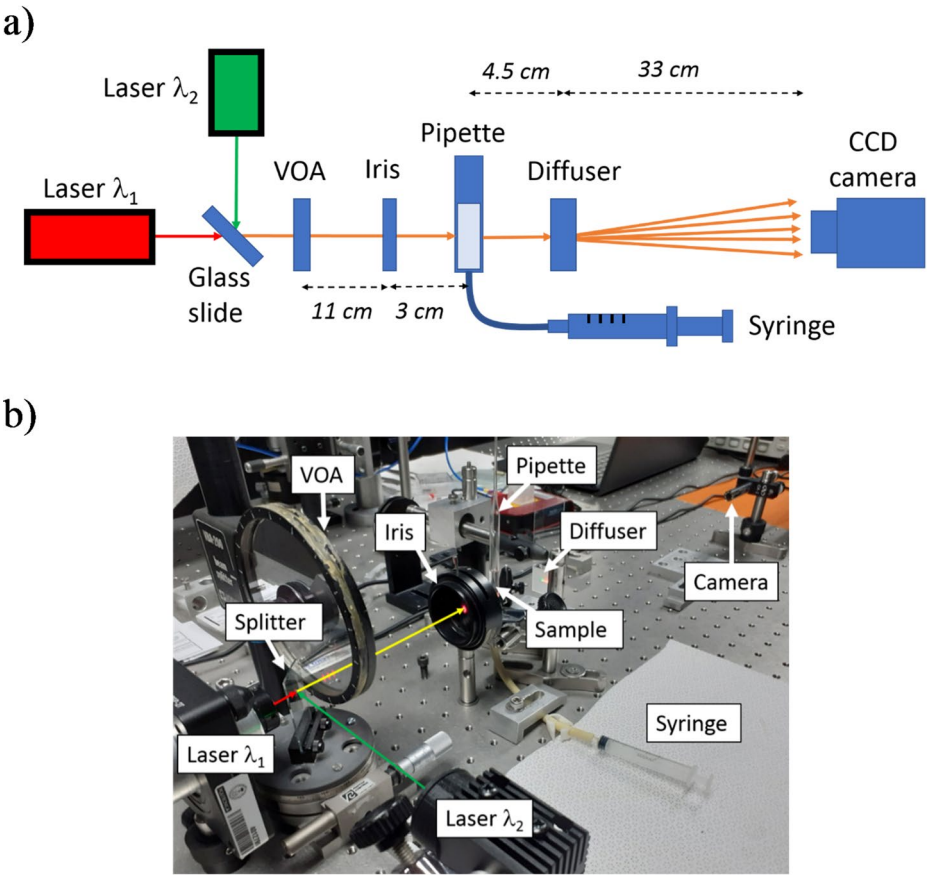

Fig. 1 Schematic front view (**a**) and photograph (**b**) of the free-space dual-wavelength speckle-based optical system for salinity sensing of aqueous solutions. The optical paths of the laser beams at λ_1 (635 nm) and λ_2 (532 nm) and the two-wavelength merged beam are indicated by red, green and yellow arrows, respectively, in the photograph

shape the cross-section of the combined beam striking the pipette into a ~ 1.5 mm-diameter beam spot. The beam passing the pipette was incident on a ground glass diffuser (frosted microscope glass slide) separated 4.5 cm from the pipette. A CCD camera, positioned at 33 cm from the diffuser and connected to a laptop, was utilized to monitor the central region of the transmitted speckle pattern. Speckle digital images were captured at a resolution of 640 × 480 pixels in the RGB color format. A Matlab program was developed and executed on the laptop to display and record the speckle images and to calculate, in real time, the correlation coefficients for the individual color components.

The correlation coefficient (C) for a given color component between the speckle pattern of the sample under test and that of a reference sample is calculated as (Woods and Gonzalez 2021):

$$C = \frac{\sum_{i=1}^{N}\sum_{j=1}^{M}\left[I_R(i,j) - \bar{I}_R\right]\left[I_S(i,j) - \bar{I}_S\right]}{\sqrt{\left\{\sum_{i=1}^{N}\sum_{j=1}^{M}\left[I_R(i,j) - \bar{I}_R\right]^2\right\}\left\{\sum_{i=1}^{N}\sum_{j=1}^{M}\left[I_S(i,j) - \bar{I}_S\right]^2\right\}}} \quad (1)$$

where N and M are the digital image dimensions in pixels, $I_R(i,j)$ and $I_S(i,j)$ are the color-component intensities at the pixel (i, j) of the reference and sample speckle patterns, respectively, and $\bar{I}_R$ and $\bar{I}_S$ are the corresponding mean values. The correlations for the red and green components were calculated from the respective channels of the standard 3-channel RGB image recorded by the CCD camera. After acquisition, the Matlab program extracted each color plane (R, G, and B) from the 640 × 480 image, and the spatial correlation coefficient was computed independently for each channel according to Eq. (1).

The sensor response was calibrated using 2 mL solutions of NaCl (≥99%, Sigma-Aldrich) in distilled water, with solution concentrations ranging from 0% to 2% wt. Prior to the introduction of each calibration sample, a reference image of a speckle pattern corresponding to distilled water was recorded. The correlation coefficient was then calculated using this reference image. For each calibration sample, 300 correlation coefficient measurements were taken at an interval of 1.2 s between each measurement. The pipette was then cleaned by injecting and extracting distilled water four times. To assess reproducibility, three calibration experiments were conducted, and all measurements were recorded in darkness at room temperature (22 °C).

3 Results and discussion

Figure 2a illustrates the measured correlation coefficients for the considered concentrations of NaCl solutions, for the red (R) and green (G) color components of the recorded speckle images, as a function of time. Figure 2b shows the temporal behavior of the product of the correlation coefficients for the red and green components. It is observed in Fig. 2a that following the introduction of the sample into the pipette, signal fluctuations emerge, which can be attributed to flow currents and turbulence within the liquid due to the process of sample injection. After a transient period of approximately 150 s, the signals reach a steady state and become highly stable. A comparison of Fig. 2a and b reveals that the output signal range (the total variation in the sensor's output signal) increases for the product signal in comparison to that for the red and green components. Specifically, the output signal span for the red and green components ranges from 1 to approximately 0.2, whereas for the product ranges from 1 to approximately 0.05. This is a significant benefit of utilizing the combined product signal as opposed to the correlation coefficient of a single color component.

Figure 3 shows recorded speckle patterns following signal stabilization for different concentrations of NaCl solutions. The presence of well-resolved speckles indicates conformity with the Nyquist sampling theorem, which stipulates that the size of the speckles should exceed twice the pixel size. Furthermore, a discernible variation in the spatial intensity distribution of the combined speckle pattern, formed by the mixing of red and green colors, is observed as a function of the concentration of NaCl. The elongated shape of the speckles is due to the cylindrical shape of the sample container, which acts as a cylindrical lens.

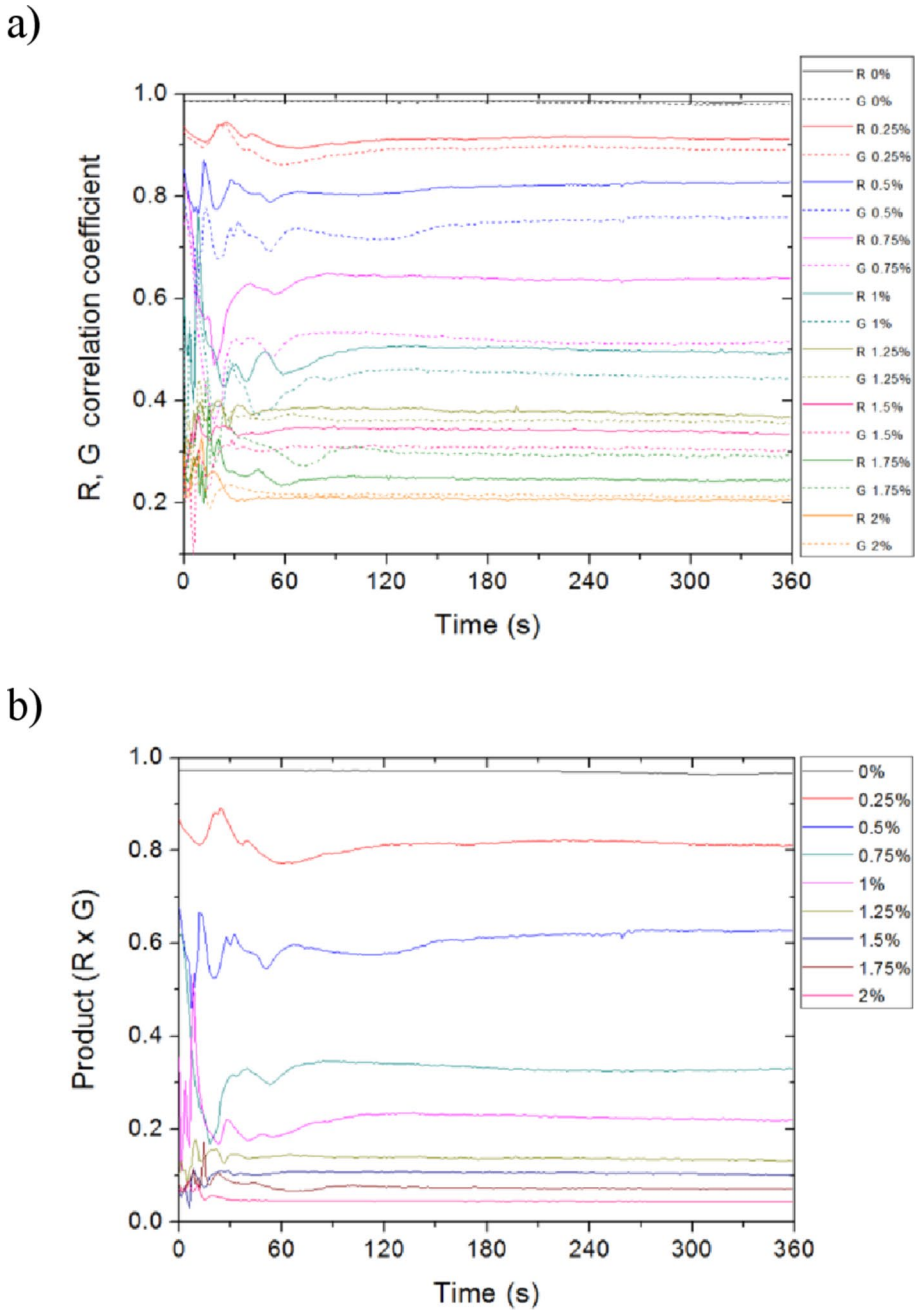

Fig. 2 Temporal evolution of the correlation coefficients for aqueous solutions of NaCl (0%, 0.25%, 0.5%, 0.75%, 1%, 1.25%, 1.5%, 1.75%, and 2%) for **a** red (R) and green (G) components of the recorded speckle images and **b** the product of the correlation coefficients of red and green color components

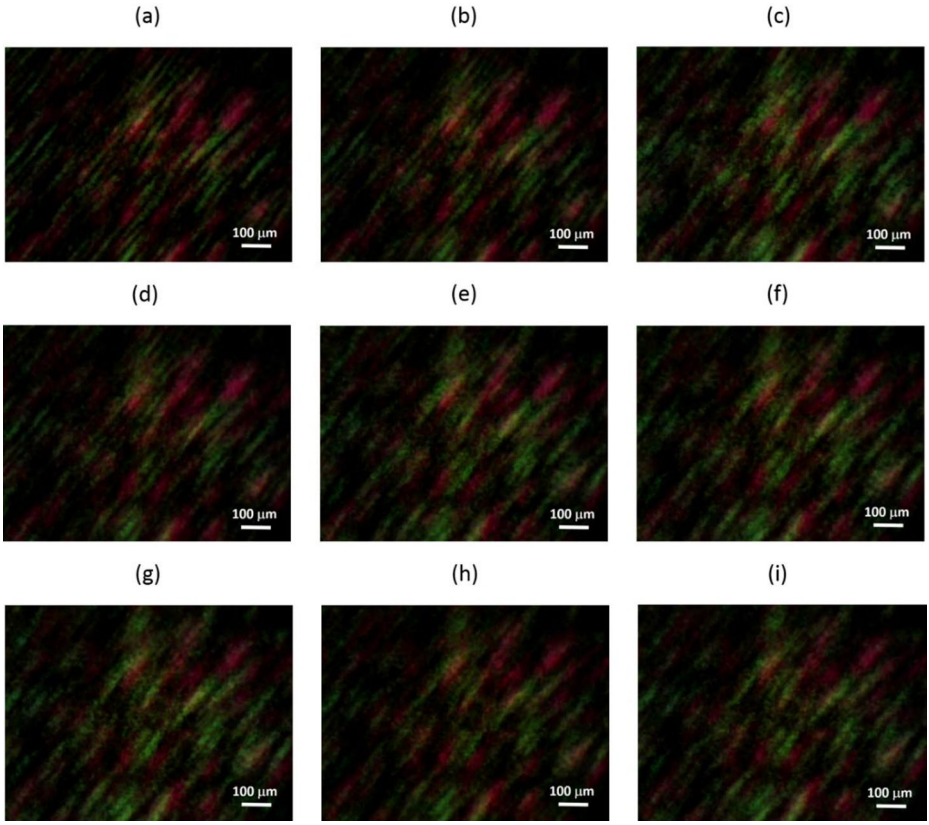

Fig. 3 Captured dual-wavelength speckle pattern images corresponding to various aqueous solutions of NaCl: **a** distilled water, **b** 0.25%, **c** 0.5%, **d** 0.75%, **e** 1%, **f** 1.25%, **g** 1.5%, **h** 1.75%, and **i** 2%. Intensity scale is the same for all images

Table 1 presents the measured data used to determine the calibration functions of the sensing system for the red, green and product signals, as well as the assessment of repeatability and reproducibility for three calibration experiments. Repeatability was evaluated for each calibration sample by calculating the standard deviation (σ_r) of 50 consecutive measurements of C after signal stabilization (from time = 300 s to time = 360 s). As shown in Table 1, the standard deviation (σ_r), which quantifies the experimental noise of the system, ranges from 10^{-4} to 10^{-3} for the red, green and product signals. These small values indicate that the experimental setup is highly stable. It is important to note that the σ_r value for the product signal remains within the same order of magnitude as those for the red and green components, indicating that the noise level of the sensing configuration is maintained when the product signal is considered. This is illustrated in Fig. 4, which shows the standard deviation (σ_r) values for all tested NaCl concentrations for the red, green, and product signals corresponding to Experiment 2 (Table 1). It is also seen in Table 1 that the standard deviation of reproducibility (σ_R), which accounts for the variability among the results of the three calibration experiments, is found to be on the order of $10^{-3} - 10^{-2}$, which supports the reliability of the experimental procedure.

Table 1 Measured values of the correlation coefficient for various aqueous solutions of NaCl for the red and green components of the speckle images and the product signal

Sample concentration (% wt)	C Experiment 1 $mean_1 \pm \sigma_r$	C Experiment 2 $mean_2 \pm \sigma_r$	C Experiment 3 $mean_3 \pm \sigma_r$	C Reproducibility MEAN $\pm \sigma_R$
RED				
0	$0.9862 \pm 4 \cdot 10^{-4}$	$0.9852 \pm 3 \cdot 10^{-4}$	$0.9845 \pm 3 \cdot 10^{-4}$	$0.9853 \pm 9 \cdot 10^{-4}$
0.25	$0.8901 \pm 2.8 \cdot 10^{-3}$	$0.8991 \pm 8 \cdot 10^{-4}$	$0.9117 \pm 6 \cdot 10^{-4}$	$0.9003 \pm 1.1 \cdot 10^{-2}$
0.5	$0.7996 \pm 9 \cdot 10^{-4}$	$0.8058 \pm 7 \cdot 10^{-4}$	$0.8265 \pm 6 \cdot 10^{-4}$	$0.8106 \pm 1.4 \cdot 10^{-2}$
0.75	0.6391 ± 10^{-3}	$0.6543 \pm 1.9 \cdot 10^{-3}$	$0.6348 \pm 3.4 \cdot 10^{-4}$	0.6427 ± 10^{-2}
1	$0.5047 \pm 2.1 \cdot 10^{-3}$	$0.4949 \pm 1.9 \cdot 10^{-3}$	$0.5470 \pm 1.8 \cdot 10^{-3}$	$0.5155 \pm 2.7 \cdot 10^{-2}$
1.25	$0.3551 \pm 1.7 \cdot 10^{-3}$	$0.3718 \pm 2.2 \cdot 10^{-3}$	$0.4046 \pm 1.4 \cdot 10^{-3}$	$0.3772 \pm 2.5 \cdot 10^{-2}$
1.5	$0.3159 \pm 1.2 \cdot 10^{-3}$	$0.3375 \pm 2.3 \cdot 10^{-3}$	$0.3419 \pm 1.1 \cdot 10^{-3}$	$0.3318 \pm 1.4 \cdot 10^{-2}$
1.75	$0.2201 \pm 1.4 \cdot 10^{-3}$	0.2441 ± 10^{-3}	$0.2557 \pm 1.1 \cdot 10^{-3}$	$0.2399 \pm 1.8 \cdot 10^{-2}$
2	$0.1996 \pm 9 \cdot 10^{-4}$	$0.2060 \pm 9 \cdot 10^{-4}$	$0.2062 \pm 9 \cdot 10^{-4}$	$0.2039 \pm 3.7 \cdot 10^{-3}$
GREEN				
0	$0.9833 \pm 1.3 \cdot 10^{-3}$	$0.9833 \pm 7 \cdot 10^{-4}$	$0.9798 \pm 8 \cdot 10^{-4}$	$0.9821 \pm 2 \cdot 10^{-3}$
0.25	$0.8593 \pm 3.7 \cdot 10^{-3}$	$0.8704 \pm 1.9 \cdot 10^{-3}$	$0.8911 \pm 9 \cdot 10^{-4}$	$0.8736 \pm 1.6 \cdot 10^{-2}$
0.5	$0.7386 \pm 1.3 \cdot 10^{-3}$	0.7341 ± 10^{-3}	$0.7589 \pm 1.1 \cdot 10^{-3}$	$0.7439 \pm 1.3 \cdot 10^{-2}$
0.75	$0.5129 \pm 1.6 \cdot 10^{-3}$	$0.5616 \pm 1.9 \cdot 10^{-3}$	$0.5709 \pm 3.3 \cdot 10^{-3}$	$0.5485 \pm 3.1 \cdot 10^{-2}$
1	$0.4684 \pm 1.5 \cdot 10^{-3}$	$0.4453 \pm 1.5 \cdot 10^{-3}$	$0.4764 \pm 1.2 \cdot 10^{-3}$	$0.4634 \pm 1.6 \cdot 10^{-2}$
1.25	$0.3569 \pm 1.8 \cdot 10^{-3}$	$0.3589 \pm 1.5 \cdot 10^{-3}$	$0.3647 \pm 1.7 \cdot 10^{-3}$	$0.3602 \pm 4 \cdot 10^{-3}$
1.5	$0.2914 \pm 1.9 \cdot 10^{-3}$	$0.3042 \pm 1.2 \cdot 10^{-3}$	$0.3141 \pm 1.3 \cdot 10^{-3}$	$0.3033 \pm 1.1 \cdot 10^{-2}$
1.75	$0.2964 \pm 1.2 \cdot 10^{-3}$	$0.2922 \pm 1.3 \cdot 10^{-3}$	$0.2932 \pm 1.1 \cdot 10^{-3}$	$0.2939 \pm 2.2 \cdot 10^{-3}$
2	$0.2079 \pm 1.3 \cdot 10^{-3}$	0.2059 ± 10^{-3}	$0.2133 \pm 1.1 \cdot 10^{-3}$	$0.2091 \pm 3.8 \cdot 10^{-3}$
PRODUCT				
0	$0.9698 \pm 1.6 \cdot 10^{-3}$	$0.9687 \pm 1.1 \cdot 10^{-3}$	$0.9647 \pm 1.1 \cdot 10^{-3}$	$0.9677 \pm 2.7 \cdot 10^{-3}$
0.25	$0.7649 \pm 5.7 \cdot 10^{-3}$	$0.7826 \pm 2.2 \cdot 10^{-3}$	$0.8124 \pm 1.1 \cdot 10^{-3}$	$0.7866 \pm 2.3 \cdot 10^{-2}$
0.5	$0.5906 \pm 1.4 \cdot 10^{-3}$	$0.5915 \pm 1.1 \cdot 10^{-3}$	$0.6273 \pm 1.1 \cdot 10^{-3}$	$0.6031 \pm 2.1 \cdot 10^{-2}$
0.75	$0.3278 \pm 1.4 \cdot 10^{-3}$	$0.3675 \pm 2.1 \cdot 10^{-3}$	$0.3625 \pm 3.9 \cdot 10^{-3}$	$0.3526 \pm 2.1 \cdot 10^{-2}$
1	$0.2364 \pm 1.4 \cdot 10^{-3}$	$0.2204 \pm 1.4 \cdot 10^{-3}$	$0.2606 \pm 1.2 \cdot 10^{-3}$	$0.2391 \pm 2 \cdot 10^{-2}$
1.25	$0.1268 \pm 1.1 \cdot 10^{-3}$	$0.1335 \pm 1.2 \cdot 10^{-3}$	$0.1475 \pm 9 \cdot 10^{-4}$	0.1359 ± 10^{-2}
1.5	$0.0921 \pm 8 \cdot 10^{-4}$	0.1027 ± 10^{-3}	$0.1074 \pm 6 \cdot 10^{-4}$	$0.1007 \pm 7.8 \cdot 10^{-3}$
1.75	$0.0652 \pm 5 \cdot 10^{-4}$	$0.0713 \pm 5 \cdot 10^{-4}$	$0.0749 \pm 5 \cdot 10^{-4}$	$0.0705 \pm 4.9 \cdot 10^{-3}$
2	$0.0415 \pm 3 \cdot 10^{-4}$	$0.0424 \pm 3 \cdot 10^{-4}$	$0.04397 \pm 3 \cdot 10^{-4}$	$0.0426 \pm 1.2 \cdot 10^{-3}$

σ_r is the repeatability standard deviation of 50 consecutive measurements after signal stabilization. MEAN and σ_R are the mean value and the reproducibility standard deviation, respectively, of the mean values of Experiment 1 ($mean_1$), Experiment 2 ($mean_2$) and Experiment 3 ($mean_3$)

Assuming that, for a given NaCl concentration, the red and green signals behave as normally-distributed random variables with means μ_R and μ_G and standard deviations σ_R and σ_G, respectively, the variance of their product for small values of σ_R and σ_G can be approximated as (Papoulis 1965):

$$\sigma_P^2 \approx \mu_R^2 \sigma_G^2 + \mu_G^2 \sigma_R^2 + 2\mu_R \mu_G Cov(R, G) \tag{2}$$

where Cov(R, G) is the covariance of both signals. If the red and green signals are uncorrelated, then Cov(R, G) = 0, and Eq. 1 becomes:

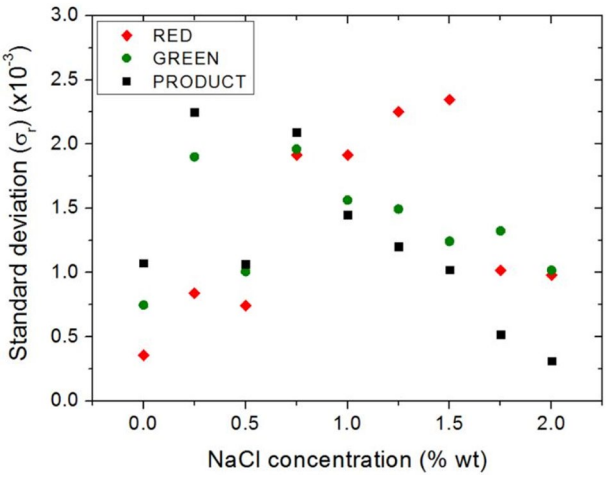

Fig. 4 Standard deviation of the measured correlation coefficient (C) for the tested aqueous concentrations of NaCl for red (red rhombic dots), green (green circle dots), and product (black square dots) signals corresponding to Experiment 2. All standard deviation values were calculated for 50 measurements of C after signal stabilization

$$\sigma_P^2 \approx \mu_R^2 \sigma_G^2 + \mu_G^2 \sigma_R^2 \tag{3}$$

According to Eq. 3, the standard deviation of the product can be reduced to a value smaller than the standard deviation of the individual signals if the following conditions are met (see Supplementary Information):

$$\mu_G^2 + \mu_R^2 \frac{\sigma_G^2}{\sigma_R^2} < 1 \tag{4}$$

$$\mu_R^2 + \mu_G^2 \frac{\sigma_R^2}{\sigma_G^2} < 1 \tag{5}$$

For the sake of illustration, if $\mu_R = \mu_G = \mu$ and $\sigma_R = \sigma_G$, then the condition for $\sigma_P < \sigma_R$, σ_G becomes $\mu < 0.7$. As illustrated in Fig. 4, the measured σ_P is observed to be larger than both σ_R and σ_G for concentrations of 0 and 0.25%. For concentrations of 0.5% and 0.75%, σ_P is approximately equal to σ_R and σ_G, and for concentrations greater than 0.75%, σ_P is smaller. This behavior approximately meets the $\mu < 0.7$ condition, where μ is the mean value of the red and green channels compiled in Table 1. This finding suggests that the noise levels of the red and green signals are significantly uncorrelated, which is consistent with the expected behavior of independent laser sources.

It is also interesting to analyze the product signal noise in case the two signals to be combined originate from a single laser source, which could be implemented using a beam splitter. The two signals would then be correlated, meaning $\mathrm{Cov}(R, G) = \sigma_R \sigma_G$ (Papoulis 1965). From Eq. 2, this leads to a standard deviation for the product signal of (see Supplementary Information):

$$\sigma_P \approx \mu_R \sigma_G + \mu_G \sigma_R \tag{6}$$

Typically, Eq. 6 results in a larger standard deviation for the product compared to the uncorrelated case. To illustrate, if $\mu_R = \mu_G = \mu$ and $\sigma_R = \sigma_G = \sigma$, then $\sigma_P \approx \sqrt{2}\mu\sigma$ for uncorrelated

signals, and $\sigma_P \approx 2\ \mu\sigma$ for correlated signals. Therefore, the implementation of the proposed combined product signal procedure is most efficiently achieved by utilizing independent light sources.

Figure 5 displays the calibration curves of the sensing system for the red, green and product correlation signals corresponding to Experiment 2. Sigmoidal fit was applied to the data points. The adjusted R^2 of the fits were 0.998, 0.995 and 0.998 for red, green and product signals, respectively. Note that the product signal can be fitted to a sigmoidal curve with high accuracy, with an adjusted R^2 similar to or even higher than those of the single color channels. The sensitivity of the sensor is defined as the derivative of the sensor response with respect to the measurand. The differentiation of the sigmoidal fit curves shown in Fig. 5 results in nonlinear negative sensitivity functions with maximum absolute values of 0.593, 0.576 and 0.853, for the red, green and product signals, respectively, occurring at NaCl concentrations of 0.80%, 0.52% and 0.42%, respectively. It is important to note that the sensitivity of the product signal is 44% and 48% higher than that of the red and green components, respectively. The limit of detection (LOD) is defined as $LOD = 3\sigma_r/S_{max}$, where σ_r is the standard deviation due to the noise system and S_{max} is the absolute value of the maximum sensitivity. Considering the measured σ_r values (Table 1) closest to the NaCl concentrations at which the highest sensitivities are obtained, the LODs for red, green and product signals are 0.0096%, 0.0052% and 0.0039%, respectively. Table 2 summarizes the main performance parameters of the sensor system for the three calibration experiments. For all experiments, the measured data fit well to sigmoidal curves (Adj. R^2 values close to 1), and the sensitivity for the product signal is greater than that for the individual components, while maintaining similar noise levels, resulting in lower LOD values.

The use of a sigmoidal fitting model in this work is empirical in the sense that it is chosen for its accuracy rather than derived from a closed-form theoretical expression. However, a sigmoidal-like trend is qualitatively expected: in speckle-based refractometry, the correlation coefficient typically remains high for small refractive-index changes, then drops rapidly once the accumulated phase shift approaches the decorrelation threshold, and finally saturates at low values. This characteristic transition produces a curve that is qualitatively similar to an S-shaped dependence. Consistent with this behavior, each of the two individ-

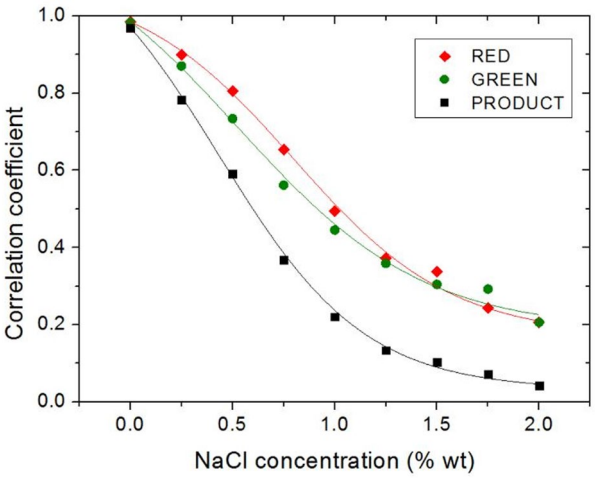

Fig. 5 Correlation coefficient as a function of the NaCl concentration for red (red rhombic dots), green (green circle dots) and product (black square dots) signals. The data points are larger than the error bars (±standard deviation of 50 measurements). Red, green and black lines represent corresponding sigmoid fits of the measured data

Table 2 Main performance parameters of the salinity sensor system for three calibration experiments

	Experiment 1				Experiment 2				Experiment 3			
	S_{max} (/%)	σ_r	LOD (%)	Adj R^2	S_{max} (/%)	σ_r	LOD (%)	Adj R^2	S_{max} (/%)	σ_r	LOD (%)	Adj R^2
R	−0.594 @ 0.76%	10^{-3}	0.0050	0.996	−0.593 @ 0.80%	$1.9 \cdot 10^{-3}$	0.0096	0.998	−0.543 @ 0.80%	$3.4 \cdot 10^{-3}$	0.0187	0.993
G	−0.601 @ 0.44%	$1.3 \cdot 10^{-3}$	0.0065	0.983	−0.576 @ 0.52%	10^{-3}	0.0052	0.995	−0.588 @ 0.60%	$1.1 \cdot 10^{-3}$	0.0056	0.992
P	−0.887 @ 0.40%	$1.4 \cdot 10^{-3}$	0.0047	0.995	−0.853 @ 0.42%	$1.1 \cdot 10^{-3}$	0.0039	0.998	−0.869 @ 0.50%	$1.1 \cdot 10^{-3}$	0.0038	0.996

R ≡ red component. G ≡ green component. P ≡ product. S_{max} ≡ maximum absolute value of the sensitivity. LOD ≡ limit of detection. Adj. R^2 ≡ adjusted coefficient of determination for a sigmoidal fit to experimental data. σ_r is the standard deviation for 50 measurements after signal stabilization

ual correlation-versus-concentration curves obtained with the different laser sources is well described by a sigmoidal function. When these two metrics are multiplied to form the product signal, the combined response accentuates the same saturation behavior and naturally preserves a sigmoidal shape. Thus, the sigmoidal fit provides a convenient and accurate analytical representation of all three response curves, enabling reliable interpolation across the full 0–2% NaCl measurement range.

It should be noted that, although a sigmoidal fit better represents the calibration curve corresponding to the product signal over the entire 0–2% concentration range, the product response is highly linear within the 0–1% interval. The adjusted R^2 of a linear fit in this region for the product data points shown in Fig. 5 equals 0.998. The choice between a linear or sigmoidal calibration therefore depends on the intended application context. For routine measurements within the low-salinity regime—where the sensor offers its highest sensitivity—a linear calibration provides a simpler and equally accurate alternative. The sigmoidal fit is used only when describing or comparing the complete response curve and is not required for operation within the linear region.

While the primary objective of this work is to illustrate the advantages of utilizing a combined product function in comparison to the correlation coefficient of a single wavelength in the specified speckle-based sensing system, it is worthwhile to examine the performance of the studied configuration in relation to other salinity optical sensors. Table 3 shows a performance comparison of various salinity sensors of relevance based on optical technologies. The detection limit of the configuration analyzed in this work improves those exhibited by other optical approaches based on laser beam displacement and optical fiber-based configurations, and it is comparable to the lowest LOD provided by a Sagnac interferometer sensor (Wu et al. 2011). A comparison of the sensitivity of different optical techniques is complicated because of the use of different units; however, a direct comparison can be made with another speckle-based salinity sensor reported in (Lin et al. 2021) in a fiber-optic configuration. The authors of that study reported a sensitivity of −0.01086/% with a dynamic range of 0–20%. The sensitivity of the free-space sensing system presented here is approximately 80 times higher, although this improvement is achieved at the expense of a smaller dynamic range.

As a result, the proposed sensor is best suited for applications in which resolving small concentration changes around a known operating point is more important than spanning the full salinity spectrum. Because the system measures relative variations with respect to a reference sample, users can position the concentration region of interest within the optimal response interval even though the absolute measurable range remains narrow. This makes the present design particularly effective for low-salinity monitoring, controlled laboratory processes, and situations requiring high-resolution detection of small fluctuations. Conversely, applications requiring a broad salinity range, such as direct seawater measurements, would be less compatible with this configuration and may require alternative sensing approaches. This sensitivity–range trade-off therefore defines the operational context in which the proposed sensor provides the greatest benefit.

A further consideration is that, although NaCl was chosen as a model system due to its relevance, other salts in real-world waters, such as KCl, $MgCl_2$, and $CaCl_2$, exhibit distinct refractive-index increments (Chen et al. 2017). Notably, divalent ions such as Mg^{2+} and Ca^{2+} contribute more strongly to refractive-index changes per unit concentration due to their higher ionic polarizabilities and hydration characteristics (Ding et al. 2017). These differences may lead to small but systematic deviations in speckle-derived metrics relative

Table 3 Comparison table of various relevant optical salinity sensors

Sensing scheme	Sensitivity	LOD	Dynamic range	Refs.
Beam displacement	240 μm/%	0.041%	0–5%	Zhao et al. (2003a)
SPR	<2000 pm/%	0.02%	2.8–4.8%	Gentleman and Booksh (2006)
U-shaped fiber	0.42 mV/%	Not available	0–3.5%	Wang and Chen (2012)
Grating fiber	−66.1 pm/%	0.13%	0–1.5%	Possetti et al. (2009)
Sagnac interferometer	19.5 nm/%	0.001%	0–4%	Wu et al. (2011)
Two-core fiber	<2600 pm/%	0.041%	0–6%	Guzman-Sepulveda et al. (2013)
Fiber speckle	-0.01086/%	Not available	0–20%	Lin et al. (2021)
Speckle & lensing	−0.853/%	0.004%	0–2%	This work

to NaCl-only calibration. Additional contributions can arise from composition-dependent changes in scattering behavior, as mixed-salt solutions have been shown to exhibit different optical scattering signatures compared with pure NaCl solutions of equivalent concentration (Zhang et al. 2009). Such effects indicate that, in practical applications, calibration should ideally be performed using representative mixed-ion matrices that match the intended environment (e.g., seawater or brackish water). Future work will extend the present analysis by evaluating sensor performance in saltwater mixtures to quantify these composition-dependent effects.

It should be also noted that, in addition to the possibility of defining a combined product signal to enhance sensitivity, the availability of the red and green signals also offers the advantage of redundancy and cross-checking information. This is particularly relevant in the context of fault detection, outlier rejection, and data validation, contributing significantly to the reliability and robustness of the sensor system.

4 Conclusions

A multiplicative fusion function has been proposed as a sensing signal for a free-space optical system for salinity sensing based on dual-wavelength laser speckle correlation. The sample of interest is probed by two collinear laser beams at different wavelengths (red and green), generating a speckle image that is dependent on the sample NaCl concentration. The product of the correlation coefficients for the red and green components of the speckle pattern defines a new sensing signal that improves the sensor performance compared to the use of the correlation coefficient of a single wavelength channel. Specifically, these improvements include enhanced sensitivity and a broader output signal range. In addition, the combined product signal exhibits a high degree of linearity in the concentration range of 0–1%. The system's sensitivity, as determined by the combined product signal, is −0.853/% and its limit of detection is 0.004%, which is 80 times more sensitive than that reported for a fiber optic speckle-based salinity sensor and comparable to the limit of detection of more complex and expensive interferometer-based salinity sensors. The performance advantages and simplicity of the proposed combined product signal, in conjunction with the redundancy and cross-checking capability offered by a two-channel interrogation system, position the studied dual-wavelength speckled-based sensing system as a suitable tool for salinity sensing in key socio-economic sectors.

Supplementary Information The online version contains supplementary material available at https://doi.org/10.1007/s11082-026-08711-9.

Author contributions Carlos Angulo Barrios performed the study conception and design, built the optical setup, conducted the experimental characterization, collected and analyzed the data, and wrote the manuscript.

Funding Open Access funding provided thanks to the CRUE-CSIC agreement with Springer Nature. This work was supported by the Ministry of Science, Innovation and Universities of Spain under the Generation of Knowledge 2024 program (Grant number PID2024-158642OB-I00).

Data availability The datasets generated during and/or analyzed during the current study are available from the corresponding author on reasonable request.

Declarations

Competing interests The authors declare no competing interests.

References

Arı, F., Şerbetçi, H., Navruz, İ: Tapered fiber optic refractive index sensor using speckle pattern imaging. Optical Fiber Technology (2023). https://doi.org/10.1016/j.yofte.2023.103366

Barker, D.B., Fourney, M.E.: Measuring fluid velocities with speckle patterns. Optics letters **1**(4), 135–137 (1977)

Barrios, C.A.: Highly sensitive refractometric sensing system based on the combination of lensing and laser speckle correlation. Optics and Lasers in Engineering **177**, 108122 (2024)

Brul, S., Coote, P.: Preservative agents in foods: mode of action and microbial resistance mechanisms. International journal of food microbiology **50**(1–2), 1–17 (1999)

Carminati, M., Luzzatto-Fegiz, P.: Conduino: Affordable and high-resolution multichannel water conductivity sensor using micro USB connectors. Sens. Actuators B. **251**, 1034–1041 (2017)

Chen, W., Feng, F., Chen, D., Lin, W., Chen, S.C.: Precision non-contact displacement sensor based on the near-field characteristics of fiber specklegrams. Sens. Actuators A: Phys. **296**, 1–6 (2019)

Chen, Y., et al.: Wavelength and concentration-dependent optical constants of NaCl, KCl, $MgCl_2$, $CaCl_2$, and Na_2SO_4 multi-component mixed-salt solutions. Appl. Opt. **56**(27), 7662–7671 (2017)

Cloete, N.A., Malekian, R., Nair, L.: Design of smart sensors for real-time water quality monitoring. IEEE access **4**, 3975–3990 (2016)

de Felippe, J., J., T., Velasco, I.T., Lopes, O.U.: Treatment of refractory hypovolaemic shock by 7·5% sodium chloride injections. The Lancet **316**(8202), 1002–1004 (1980)

Ding, H., et al.: Accurate determination of ion polarizabilities in aqueous solutions. J. Chem. Phys. **121**(26), 6416–6424 (2017)

Facchin, M., Bruce, G.D., Dholakia, K.: Measurement of variations in gas refractive index with 10–9 resolution using laser speckle. ACS Photonics. **9**(3), 830–836 (2022)

Feng, F., Chen, W., Chen, D., Lin, W., Chen, S.C.: In-situ ultrasensitive label-free DNA hybridization detection using optical fiber specklegram. Sensors and actuators B: Chemical **272**, 160–165 (2018)

Fujiwara, E., da Evaristo Silva, L., Marques, T.H., Cordeiro, C.M.: Polymer optical fiber specklegram strain sensor with extended dynamic range. Optical Engineering **57**(11), 116107–116107 (2018)

Gentleman, D.J., Booksh, K.S.: Determining salinity using a multimode fiber optic surface plasmon resonance dip-probe. Talanta **68**(3), 504–515 (2006)

Guzman-Sepulveda, J.R., Ruiz-Perez, V.I., Torres-Cisneros, M., Sanchez-Mondragon, J.J., May-Arrioja, D.A.: Fiber optic sensor for high-sensitivity salinity measurement. IEEE photonics technology letters **25**(23), 2323–2326 (2013)

Huber, C., Klimant, I., Krause, C., Werner, T., Mayr, T., Wolfbeis, O.S.: Optical sensor for seawater salinity. Fresenius's J. Anal. Chem. **368**, 196–202 (2000)
Lin, W., Liu, B., Liu, H., Yang, C., Zhang, H.: Fibre-optic salinity sensor based on multimode fibre specklegram analysis. Meas. Sci. Technol. **32**(11), 115110 (2021)
Li, X., Liu, L., Zhao, J., Tan, J.: Optical properties of sodium chloride solution within the spectral range from 300 to 2500 Nm at room temperature. Appl. Spectrosc. **69**(5), 635–640 (2015)
Luo, D., Ma, J., Ibrahim, Z., Ismail, Z.: Etched FBG coated with polyimide for simultaneous detection the salinity and temperature. Optics Communications **392**, 218–222 (2017)
Malarde, D., Wu, Z.Y., Grosso, P., de la Tocnaye, J.D.B., Le Menn, M.: High-resolution and compact refractometer for salinity measurements. Meas. Sci. Technol. **20**(1), 015204 (2008)
Meng, Q., Dong, X., Ni, K., Li, Y., Xu, B., Chen, Z.: Optical fiber laser salinity sensor based on multimode interference effect. IEEE Sens. J. **14**(6), 1813–1816 (2014)
Nguyen, L.V., Vasiliev, M., Alameh, K.: Water salinity fiber sensor with selectable sensitivity using a liquid-fillable composite in-fiber Fabry-Perot cavity. In *7th International Symposium on High-Capacity Optical Networks and Enabling Technologies* (pp. 161–165). IEEE. (2010)
Nho, H., Tanaka, K., Kim, H.S., Watanabe, Y., Hiyama, T.: Exercise training in female patients with a family history of hypertension. European journal of applied physiology and occupational physiology **78**, 1–6 (1998)
Pan, K., Yu, F.T.: Temperature-compensated fiber specklegram strain sensing with an adaptive joint transform correlator. Applied optics **34**(19), 3823–3825 (1995)
Papoulis, A.: Random variables and stochastic processes. McGraw Hill (1965)
Pereira, D.A., Fraza˜ o, O., Santos, J.L.: Fiber Bragg grating sensing system for simultaneous measurement of salinity and temperature. Opt. Eng. **43**(2), 299–304 (2004)
Pinzon, P.J., Montero, D.S., Tapetado, A., Vazquez, C.: Dual-Wavelength Speckle-Based SI-POF Sensor for Cost-Effective Detection of Microvibrations. IEEE Journal of Selected Topics in Quantum Electronics **23**(2), 217–222 (2017)
Possetti, G.R.C., Kamikawachi, R.C., Prevedello, C.L., Muller, M., Fabris, J.L.: Salinity measurement in water environment with a long period grating based interferometer. Meas. Sci. Technol. **20**(3), 034003 (2009)
Rakova, N., Kitada, K., Lerchl, K., Dahlmann, A., Birukov, A., Daub, S., Kopp, C., Pedchenko, T., Zhang, Y., Beck, L., Johannes, B., Marton, A., Muller, D.N., Rauh, M., Luft, F.C., Titze, J.: Increased salt consumption induces body water conservation and decreases fluid intake. J. Clin. Investig. **127**(5), 1932–1943 (2017)
Ramos, P.M., Pereira, J.D., Ramos, H.M.G., Ribeiro, A.L.: A four-terminal water-quality-monitoring conductivity sensor. IEEE Trans. Instrum. Meas. **57**(3), 577–583 (2008)
Sprague, R.A.: Surface roughness measurement using white light speckle. Applied Optics **11**(12), 2811–2816 (1972)
Tran, V., Sahoo, S.K., Wang, D., Dang, C.: Utilizing multiple scattering effect for highly sensitive optical refractive index sensing. Sensors and Actuators A: Physical **301**, 111776 (2020)
Trivedi, V., Mahajan, S., Joglekar, M., Chhaniwal, V., Zalevsky, Z., Javidi, B., Anand, A.: 3D printed handheld refractometer based on laser speckle correlation. Opt. Lasers Eng. **118**, 7–13 (2019)
Wang, J., Chen, B.: Experimental research of optical fiber sensor for salinity measurement. Sensors and Actuators A: Physical **184**, 53–56 (2012)
Woods, R.E., Gonzalez, R.C.: . Digital image processing third edition. (2021)
Wu, C., Fu, H.Y., Au, H.Y., Guan, B.O., Tam, H.Y.: High-sensitivity salinity sensor realized with photonic crystal fiber Sagnac interferometer. In *21st International Conference on Optical Fiber Sensors* (Vol. 7753, pp. 224–227). SPIE. (2011)
Wu, S.H., Jin, W., Bi, W.H., Li, X., Zhang, L.K., Jin, Y.: A robust salinity sensor based on encapsulated long-period grating in microfiber. Optoelectron. Lett. **16**(6), 418–422 (2020)
Yu, Y., Bian, Q., Lu, Y., Zhang, X., Yang, J., Liang, L.: High sensitivity all optical fiber conductivity-temperature-depth (CTD) sensing based on an optical microfiber coupler (OMC). Journal of Lightwave Technology **37**(11), 2739–2747 (2019)
Zhang, X., et al.: Scattering by solutions of major sea salts. Optics Express **17**(22), 19580–5 (2009)
Zhao, Y., Liao, Y., Zhang, B., Lai, S.: Monitoring technology of salinity in water with optical fiber sensor. J. Lightwave Technol. **21**(5), 1334 (2003b)
Zhao, Y., Zhang, B., Liao, Y.: Experimental research and analysis of salinity measurement based on optical techniques. Sens. Actuators B. **92**(3), 331–336 (2003a)